https://cimav.repositorioinstitucional.mx/jspui/

Growth and microstructural study of CuO covered ZnO nanorods

F. Pola- Albores, W. Antúnez-Flores, P. Amézaga-Madrid, E. Ríos-Valdovinos, M. Valenzuela-Zapata, F. Paraguay-Delgado, M. Miki-Yoshida.

Abstract

A feasiblemethod to synthesize CuO covered ZnO nanorods was realized. Firstly, ZnO nanorods were grown by wet-chemical route at 90 °C onto borosilicate glass substrates. Subsequently, the CuO covered ZnO matrix was obtained by Aerosol-Assisted Chemical Vapor Deposition at different temperatures (300, 400, 500 and 600°C). The CuO–ZnO nanocrystals were microstructurally characterized by electron microscopy and Rietveld refinement. Results showed a CuO formed nanocrystals but also an amorphous fraction of CuO which increases with the synthesis temperature. Additionally, it was evident the presence of secondary copper-oxide phase (paramelaconite), which also has grown over the ZnO nanorod surface.

Keywords: Rietveld Refinement, AACVD process, CuO, Paramelaconite, ZnO nanorods.

Introduction

ZnO based nanomaterials are commonly used due to their interesting properties such as piezoelectric, semiconducting and high transmittance (80%≤T(λ)≤92%) at wavelengths in the visibleinfrared range (400–2500 nm) [1–3]. Zinc oxide is a widely studied n-type semiconductor, with a 3.3 eV band gap [4] and it has been used in optics, optoelectronic devices (light emitting and laser diodes), actuators, solar cells,

photocatalysis, transistors, industry and sensors. It has been synthesized by several methods and in different morphologies, including 1D geometry [5].

Sensing properties could be improved using 1D geometry due to high surface to volume ratio but also with the inclusion of other metal oxide phase. Copper oxide gives the possibility to expand functionality of ZnO semiconductor in reducing-gas sensor applications (e.g. H2, CO). Actually, bulk applications of CuO–ZnO materials are focused on heterogeneous catalysis in methanol synthesis. CuO is a transition metal oxide with p-type semiconductivity and a narrow direct band gap of 1.21–1.51 eV [6,7]; additionally, it has high absorbance below 850 nm being suitable for solar energy applications [8]. Furthermore, it is a Mott insulator, a giant magneto resistant and a superconductor material [9] being attractive for electronic devices and nanofluids [10]; industrially, CuO has great interest, as pigment, gas sensor and catalyst [11,12]. Synthesis of CuO nanoparticles has been reported by photodeposition, homogeneous co-precipitation, electrodeposition [13,14], physical/chemical vapor deposition [15] and wet chemical methods [16–18], and also impregnation and thermal decomposition [19].

Mixed oxides type CuO–ZnO have been studied in thin film geometry [20], in compressed powders [21,22] and recently as composite materials [23]; however, one-dimensional nanosized CuO–ZnO structures have not been reported.

In the present work, we report the synthesis of ZnO nanorod on a borosilicate glass substrate by chemical bath deposition and the formation of CuO nanoparticles over the ZnO nanorod by Aerosol-Assisted Chemical Vapor Deposition (AACVD). For the CuO deposition we have tried different temperatures: 300, 400, 500 and 600 °C. The formed nanostructures have been characterized in detail in terms of their

microstructural properties and crystallographic information, obtained by field emission scanning electron microscopy (SEM), high resolution transmission electron microscopy (HRTEM), X-ray and electron diffraction. Finally reaction mechanisms of CuO deposition and Cu_4O_3 formation have been proposed.

Experimental details

Synthesis of ZnO nanorods: ZnO nanorods were prepared onto borosilicate glass substrates by chemical bath deposition using colloidal ZnO seeds as nucleation centers [24]. The seeds were prepared by sol–gel method using a zinc acetate in ethanol and sodium hydroxide in methanol solution, respectively. The reaction was carried out at 60 °C in a reflux system under vigorous stirring. Cleaned borosilicate substrates (2x 1.5 cm) were immersed in the seed solution and finally they were thermally treated at 200 °C in vacuum. The ZnO nanorods were grown inside a tube cells, using the seed coated substrates and zinc nitrate 0.25 mol dm^{-3}, hexamethylenetetramine 0.5 mol dm^{-3}, polyethy-lene glycol around 10 wt.% and tridistilled water as reactants. Temperature of the reactors was controlled at 90 °Cby3hinawater bath. After this time, the substrates were washed with deionized water and finally they were calcined at 360 °C by 30min.

AACVD of copper oxide: An AACVD system was used to deposit copper oxide onto ZnO nanorods coated substrates. Oil-free, filtrated and preheated (at 28 °C) air was used as carrier gas and it was feed at constant pressure of 2.8 x 10^5 Pa to a mass flow controller (Omega-FMA1422). The controller supplied the carrier at constant flow of 3000 cm^3 min^{-1} to a nebulization chamber loaded with pre-cursor solution. Precursor solution was prepared with copper nitrate hemipentahydrate reagent grade, $Cu(NO_3)_2 \cdot 2.5H_2O$, diluted in methanol to 0.1 mol dm^{-3}. Nebulization of solution was carried out

with an ultrasonic nebulizer (Sonaer-241) oper-ated at 2.4 MHz. The ZnO nanorods coated substrates were placed at the center of Vycor glass tube inside a tubular furnace (Lindberg Blue) where the temperature was varied between 300 and 600 °C settled within ±5 °C.

The mixture gas carrier–aerosol precursor reaches the ZnO matrix in the reaction zone by a stainless steel injection nozzle (ID=0.7 cm). After deposition, effluent gases exit the tubular furnace and they were extracted by a fume hood.

Several experiments were carried out in order to optimize the reaction (deposition) time in order to reach an homogeneous and thin copper oxide layer to avoid flood effect in the ZnO matrix. The optimization was realized at 300 °C in a clean borosilicate glass substrate (without ZnO nanorods). After optimization, deposition was realized onto ZnO nanorods.

Characterization: The morphology and elemental analysis of nanostructured materials were studied by field emission scanning electron microscopy using a JEOL JSM-7401F operated at 3 keV, coupled with a X-ray energy dispersive spectroscopy (EDS) system (Inca-Oxford). Semi-quantitative analysis of metal oxides was carried out taking in consideration both, the stoichiometric proportion of oxides and the SiO2 as the main glass composition. Growing mechanism of CuO nanoparticles over the ZnO prismatic face was studied by high resolution transmission electron microscopy using a JEOL JEM-2200FS microscope operated at 200 kV. CuO–ZnO samples were prepared scratching the glass surface with a sharp cutter over a 200 mesh Ni grid. In addition, scanning transmission electron microscopy (STEM) and selected area electron diffraction (SAED) patterns were used to determine micro-structural details.

Phase identification and quantitative phase analysis were realized by grazing incidence X-ray diffraction, GIXRD, using a Panalytical XPert diffractometer configured in ω-2θ geometry, operated at 40kV and 35mA, with a Cu target X-ray generator (λK_α=0.15419nm). Incident beam optics was configured with omega (ω) settled at 1°, and the data was collected between 25 and 95° (2θ) with a step size 0.02° and a scan rate of 0.1 min^{-1}.

Rietveld refinement was realized using the FullProf software [25] considering the instrumental peak broadening in the crystallite size calculations. Crystallite sizes were computed internally by FullProf for each reflection and then averaged.

Initial structural models were obtained from files 154486.cif and 43179.cif for ZnO and CuO phases, respectively. The non-structural model considered the Thompson–Cox–Hasting pseudo-Voigt profile function. The ZnO phase was considered in proper stoichiometry and the atomic site occupancies were not refined.

Quantitative phase analysis was additionally obtained by Rietveld refinement with the profile matching mode [26]. First, pure CuO coated substrate X-ray measurement was used as reference material. Here, the tabulated moduli of structure factors were obtained (in absolute units) in a ‘hkl’ file after the refine-ment of lattice parameters, profile shape, atomic positions, Debye–Waller factor, etc. This ‘hkl’ list was used as input file for subsequent refinements of the CuO–ZnO nanomaterials so that the program reads the list of structure factor (IFl) of minor phase (CuO), instead of generating them. The ZnO phase was refined normally. Cell volume and density of each phase were calculated from refined lattice parameters using PowderCell software [27].

Results and discussion

Optimization of CuO layer: The minimum deposition temperature of CuO deposition was 300 °C, and it was determined by thermodiffraction (results not presented here). We have performed an optimization of reaction time. To accomplish this task, several deposition time of copper oxide onto bared borosilicate glass substrates was tried at 300 °C. Fig. 1(a) shows representative SEM micrograph of a CuO layer obtained at 300 °C with 6 min of aspersion. For higher reaction time (e.g. 10 min), the amount of deposited CuO would increase in excess over the exposed ZnO surface. Consequently, 6 min of aspersion was considered as the optimum time to form an adequate copper oxide layer and it was kept constant in subse-quent depositions at different temperatures. Fig. 1(b) shows a diffraction pattern of deposited monoclinic CuO nanoparticle layer onto borosilicate glass, identified as tenorite, with the PDF card 45-0937. Other phases different than tenorite were not detected.

Phase analysis of copper oxide covered ZnO nanorods: The deposition of copper oxide onto ZnO nanorods was realized between 300 and 600 °C. Fig. 2 shows diffraction patterns of CuO–ZnO nanocrystals. Phase identification showed two phases, the former identified as hexagonal ZnO wurtzite struc-ture, with space group $P6_3mc$ and lattice parameters a=0.32498 nm and c=0.52066 nm, according to PDF card 36-1451. The second phase was identified as monoclinic tenorite CuO with space group C1 2/c1, and lattice parameters a=0.46853 nm, b=0.34257 nm and c=0.51303 nm and β = 99.5490°, according to PDF card 45-0937. It is worth noting that the CuO phase was scarcely formed at 300 °C; therefore, as the precursor decomposition to form CuO is favored at high temperatures, the diffraction intensities are more evident at 500 and 600 °C.

Rietveld analysis:

Lattice parameters and crystallite size: Previous phase characterization and refinement of diffracto-gram in Fig. 1(b) was used to obtain CuO structure factors. Rietveld results are presented in Table 1. It can be observed that the refinement reached acceptable values of the goodness of fitness index (S). Also, lattice parameters a and c of ZnO phase gradually reduce, as the AACVD temperature increases from 400 to 600 °C; however, the c/a ratio and the fractional coordinate z agree with the value of the wurtzite type structure of ZnO. It is expected that the slight decrease in lattice parameters will not change the cell volumes and densities substantially.

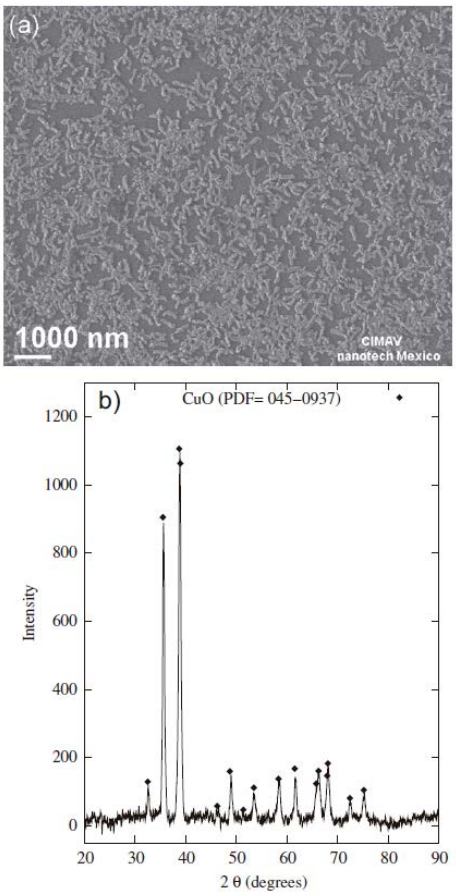

Fig. 1. (a) SEM micrograph and (b) diffraction pattern of CuO layer deposited at 300 °C over a clean glass substrate.

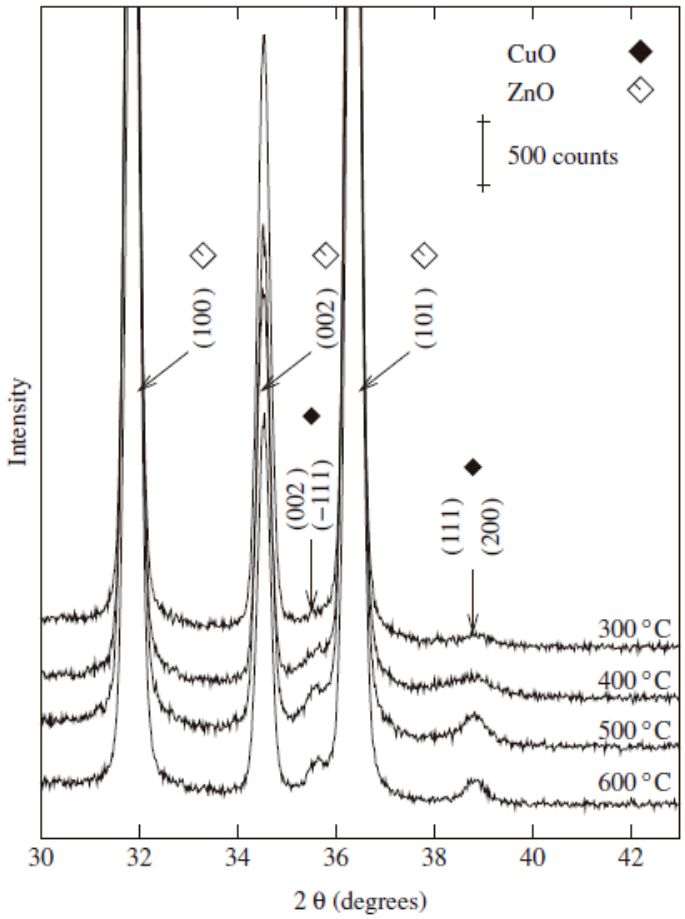

Fig. 2. Diffraction patterns of CuO covered ZnO nanorods deposited by AACVD at different temperatures.

On the other hand, refined lattice parameters of CuO tenorite phase presented in Table 1 did not show a clear tendency compared to the reference parameters at different deposition temperatures; this fact can be attributed to the low symmetry of the monoclinic cell. However, cell volume and density plotted in Fig. 3 shows the integrated temperature effect in these parameters. It is evident a compromise in the reduction in cell volume and the increase of cell density, both above the reference values.

The average crystallite sizes are tabulated in Table 1 for both, ZnO and CuO phases, respectively. ZnO nanorods synthesized by chemical route are ranging from 86 to 89 nm (and 90 nm at 300 °C, not included in the table), indicating a narrow size

distribution in the synthesis step. These results agree well with cell volume in this phase. CuO nanocrystals size vary from 11 to 41 nm, indicating that AACVD method is suitable for the synthesis of nanostructures. Additionally, the deposition temperature influences directly the nanocrystal size, as temperature increases in 100 °C, the CuO domain size increased almost twofold. The addition of CuO nanocrystals could cause inter granular potential barrier and they could modify the conducting properties of ZnO.

Quantitative phase analysis: EDS analysis was realized as a first approximation for quantitative phase analysis; these results are shown in Table 2 in comparison with X-ray refinement results. EDS spectra were obtained at low magni-fication (400 x) in several zones and the contribution of substrate was also considered in the results. This analysis gives more reliable value at 300 °C where diffraction lines are too low. It can be observed that the total CuO concentration increases with synthesis temperature, it approximates to 11 wt.% for 600 °C. According to X-ray results (data given in Table 2), only some proportion of the total amount of CuO is crystalline, and contrary to that expected, the amorphous phase weight increases with the AACVD temperature. The amorphous content varies from 35% at 300 °C to 76.6% at 600 °C. These results suggest that precursor crystallization in aerosol route could not occurs via solid-state reactions due to large differences in the heating rate.

Morphology analysis: Fig. 4 shows SEM secondary electron micrographs of CuO covered ZnO nanorods, as a function of CuO deposition temperature. The roughness evidences the deposited quantity of CuO (amorphous and crystalline). Fig 4(a) clearly shows prismatic faces of ZnO nanorods. At 300 °C the presence of copper oxide is not evident. Isolated particles were found over some planes as indicated in the figure. Fig.

4(b) shows more quantity of CuO deposited over the rods, but they still preserved their prismatic appearance. The hexagonal typical shape of ZnO rods was lost when deposition temperature increased. In Fig. 4(c) and (d) the planes f0110g were completely covered by the copper oxide; however, it can be seen uncovered rod faces below the superficial nanorods, where the aerosol precursor could not reach (see arrows). At 500 and 600 °C the roughness was very notorious due to the deposition of more CuO nanostructures; although, as it was described before, not all the deposited masses correspond to the crystalline phases.

Table 1
Rietveld refinement results for ZnO and CuO phases. *T*, deposition temperature of AACVD reaction (in °C); *Ref.*, data obtained from PDF cards *36-1451* and *45-0937* for ZnO and CuO phases, respectively; *S*, goodness of fit indicator (R_{wp}/R_{exp}); *a*, *b*, *c*: lattice parameters (in nm), β (in °); *z*†, refined atomic position of oxygen; CS, average crystallite size (in nm).

ZnO						
T	*S*	*a*	*c*	*c*/*a*	*z*†	CS
600	1.49	0.32487 ± 0.000012	0.52033 ± 0.00002	1.6017	0.3817	88 ± 11
500	1.65	0.32489 ± 0.000012	0.52034 ± 0.00002	1.6016	0.3841	86 ± 11
400	1.55	0.32491 ± 0.000012	0.52036 ± 0.00002	1.6015	0.3830	89 ± 11
Ref.		0.32498	0.52066	1.6021	0.3810	

CuO					
T	*a*	*b*	*c*	β	CS
600	0.46956 ± 0.00019	0.34189 ± 0.00012	0.51367 ± 0.00021	99.5806	41 ± 6
500	0.46889 ± 0.00019	0.34398 ± 0.00013	0.51178 ± 0.00023	99.5337	19 ± 4
400	0.46848 ± 0.00019	0.34384 ± 0.00012	0.51356 ± 0.00021	99.5575	11 ± 2
Ref.	0.46853	0.34257	0.51303	99.5490	

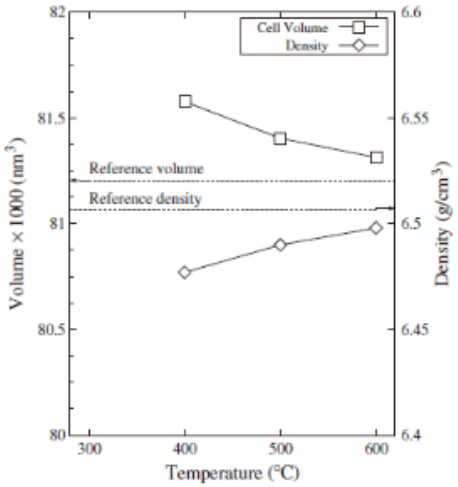

Fig. 3. Cell volumes and densities obtained from refined data as a function of CuO synthesis temperature. Reference values were calculated from reported lattice parameters in PDF card *45-0937* of tenorite.

Table 2
Results of quantitative analysis of CuO phase; m_{total} total amount of deposited CuO (balance ZnO) calculated by EDS analysis (in wt.%); m_C, crystalline part from GIXRD refinement (in wt.%); m_α, amorphous weight fraction of the total CuO phase (in wt.%), obtained by $100(1-m_C/m_{total})$.

T	m_{total}	m_C	m_α
600	10.7	2.5	76.6
500	10.3	3.7	64.3
400	6.5	4.2	35.4

Paramelaconite identification and growth mechanism: Field emission transmission electron microscopy and diffrac-tion analysis of CuO covered ZnO nanorods showed important information of their microstructure. Transmission electron micro-graphs and diffraction pattern of sample synthesized at 300 1C are shown in Fig. 5.

Fig. 5(a) shows a STEM micrograph of a low amount CuO covered nanorod; one of the zones chosen to take SAED pattern is also signaled. Indexed SAED in Fig. 5(b) reveals the presence of a copper oxide phase named paramelaconite,Cu_4O_3, wich has a tetragonal structure (141/amd, s-g. 141, a=0.58370 nm, c=0.99320 nm), indexed with JCPDS card 083-1665. Paramelaconite (Cu_4O_3)is one of the three Cu–O minerals (tenorite, CuO and cuprite, Cu_2O the others); it is a mixed oxide structure where Cu atoms are present in valences Cu^{1+} and Cu^{2+} as the form of Cu_2O . 2CuO. Thermodynamic data, semiconducting properties and formation mechanism of paramelaconite are not well understood [28–30], although some optical properties have been reported [31]. In addition, Fig. 5(c) shows lattice fringes of family planes (202) and (103), confirming the presence of the paramelaconite phase deposited onto the ZnO nanorod surface. Interestingly, the Cu_4O_3 phase has grown just over the ZnO surface,

where CuO or other copper oxide were not detected by electron diffraction. Complementary SAED patterns (not presented here) realized to samples synthesized at 400, 500 and 600 1Calsorevealthe Cu_4O_3 phase.

Paramelaconite was formed at all temperatures range between 300 and 600 1C, according to SAED patterns. However, such Cu_4O_3 phase was not detected by GIXRD, neither in diffractograms of Fig. 1(b) nor in Fig. 2. Experimental evidence suggests that Cu_4O_3 only had been formed in low quantities at local regions close to the ZnO surface.

A mechanism over the formation of paramelaconite phase is sketched in Fig. 6. First of all, CuO deposits over the ZnO phase at reaction temperature from precursor decomposition. A lattice match-ing effect between ZnO and CuO can take place simultaneous to the deposition. The lattice parameters in zincite (a'=b'=0.32498nm, c'=0.52066 nm) and tenorite (a=0.46853, b=0.34257, c=0.51303 nm) make feasible a matching higher than 98% in c/c' and 95% in b'/b. This effect could make the CuO to growth axially oriented to ZnO. Additionally, the presence of Cu^{1+} in Cu_4O_3 suggests a reduction of CuO species. At elevated temperatures, the methanol from pre-cursor solution could reduce the Cu^{2+} deposited (in CuO) to Cu^{1+} in the form of Cu_2O

$$CH_3OH_{(g)} + 6CuO \rightarrow 3Cu_2O + CO_{2(g)} + 2H_2O_{(g)} \quad (1)$$

This possibility is also supported by the thermodynamic calcula-tions of Gibbs free energy change for reaction (1): $\Delta G°_R$ (30 °C)=-339kJ/mol,$\Delta G°_R$(600°C)= 540kJ/mol [32,33]; consequently, both CuO and Cu2O phases can coexist in the ZnO surface. Finally, a solid-state reaction (2) between copper oxide species results in paramelaconite phase formation

$$2CuO+Cu_2O \rightarrow Cu_4O3 \quad (2)$$

https://cimav.repositorioinstitucional.mx/jspui/

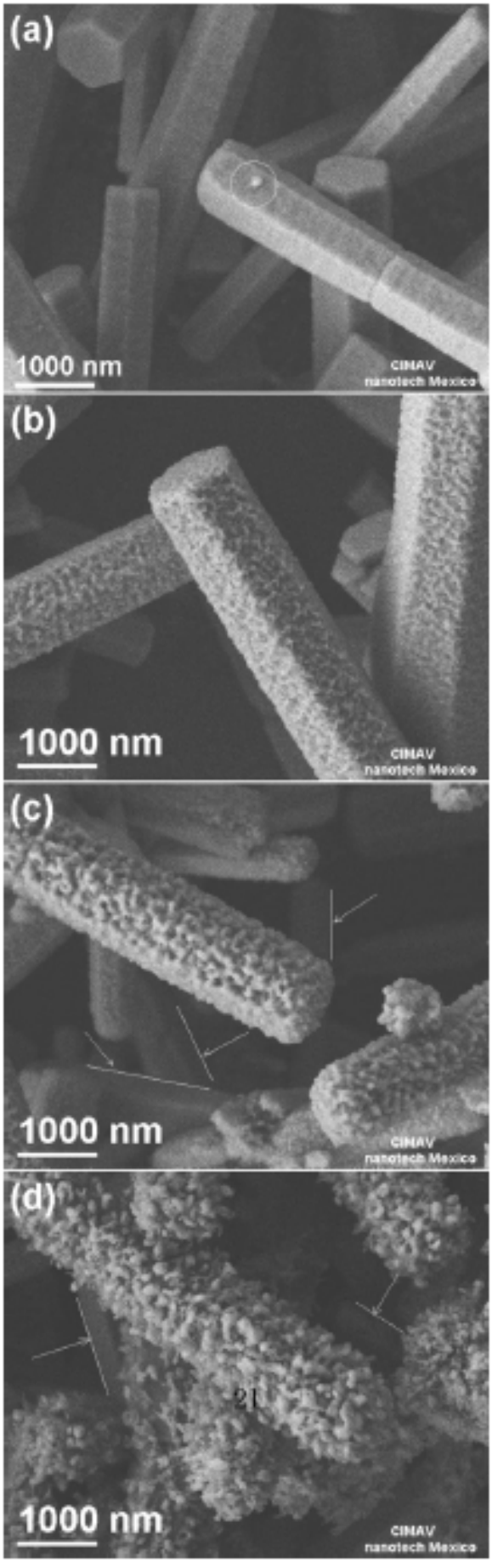

Fig. 4. SEM secondary electron micrographs of CuO deposited over ZnO nanorods at different temperatures, with a deposition time of 6 min. (a) 300, (b) 400, (c) 500 and (d) 600 °C.

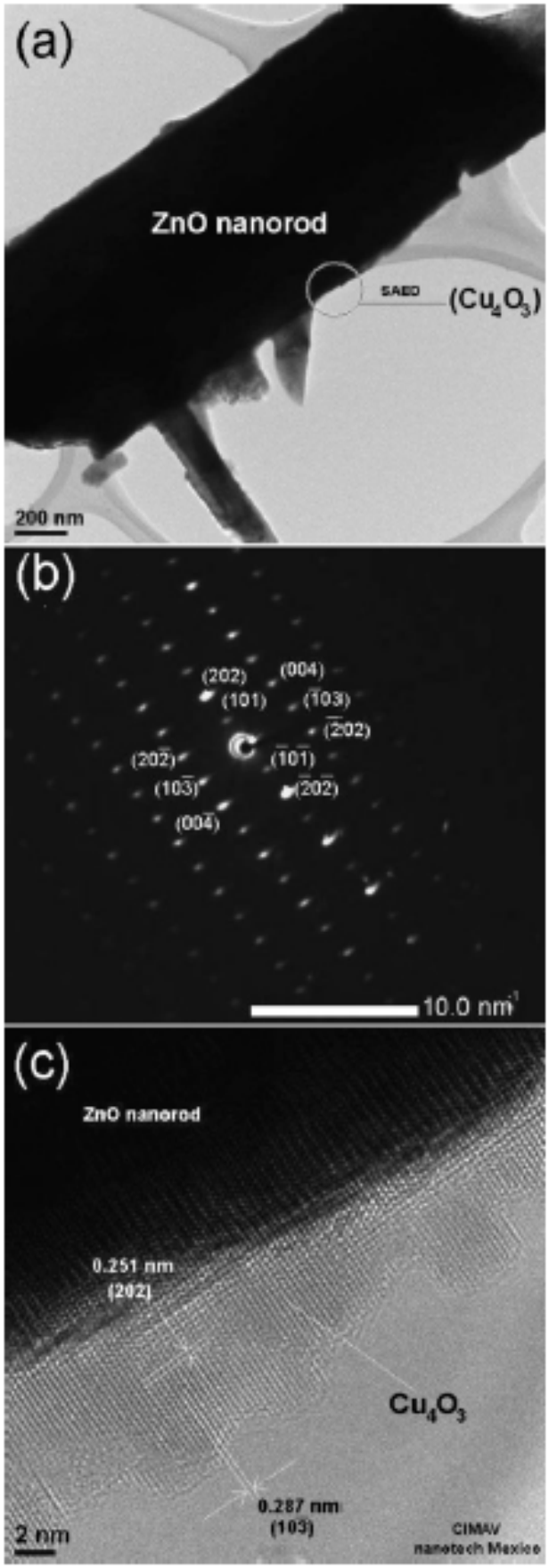

Fig. 5. (a) Bright field STEM micrograph of CuO nanocrystals over the ZnO nanorods synthesized at 300 °C. (b) Characteristic SAED pattern of zone showed in (a), denoting the existence of paramelaconite phase (Cu_4O_3). (c) High resolution STEM micrograph showing lattice fringes of (202) and (103) planes of paramelaconite deposited over a ZnO nanorod.

Conclusion

In summary, a combined method with chemical bath deposition and AACVD was used to obtain CuO–ZnO nanocrystals. Detailed microstructural characterization by Rietveld refinement resulted in the amount of CuO deposited ranged over 3–11 wt.%, as the synthesis temperature increased between 300 and 600 °C; most of the depos-ited CuO was amorphous. Further characterization by electron microscopy and diffraction showed the presence of crystalline Cu4O3 at all deposition temperatures (300–600 1C). A reaction mechanism of Cu_4O_3 formation was proposed based on three aspects: the orienta-tion of CuO over the ZnO planes, the methanol presence as reducing agent to form Cu_2O and a solid-state reaction between CuO and Cu_2O to form the paramelaconite phase over the ZnO surface.

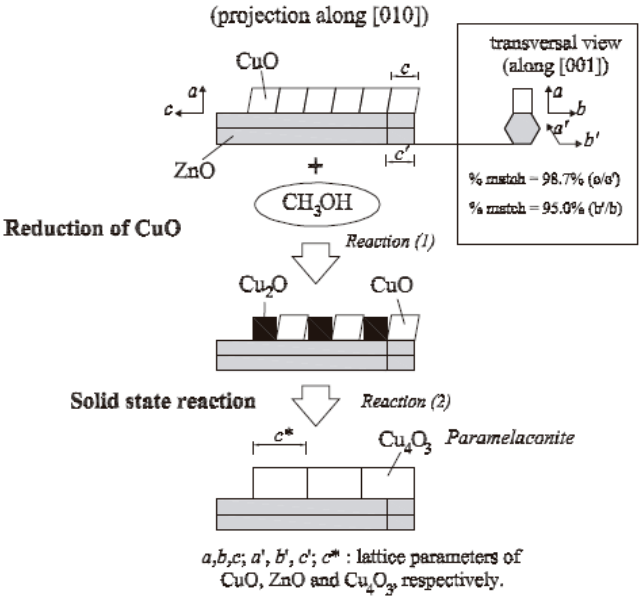

Fig. 6. Plausible mechanism of paramelaconite phase formation (Cu_4O_3) over the ZnO surface. It is evident that small differences in parameters c', c and b', b produces a high lattice matching. Cu_2O is formed by the CuO reduction with methanol prior to the Cu_4O_3 formation. In the last stage, a solid state reaction takes place between CuO and Cu_2O to complete the paramelaconite phase. Nomenclature: a, b, c; a', b', c'; c^*: lattice parameters of CuO, ZnO and Cu_4O_3, respectively.

https://cimav.repositorioinstitucional.mx/jspui/

Acknowledgments

Authors thank the technical assistance of E. Torres, C. Ornelas, O. Solís and C. Leyva in X-ray diffraction and electron microscopy analysis. This work was partially supported by prject SEP-CONACYT 2008-1-106655.

References

[1] K. Ellmer, A. Klein, B. Rech (Eds.), Transparent Conductive Zinc Oxide, Springer-Verlag, Berlin/Heidelberg, 2008., p. 273.

[2]M. Konagai, Japanese Journal of Applied Physics 50 (2011) 1–12.

[3]Z.L. Wang, Materials Science and Engineering: R 64 (2009) 64 33–71.

[4]M.H. Lai, A. Tubtimtae, M.W. Lee, G.I. Wang, International Journal of Photo-energy (2010) 1–5.

[5]X. Xu, X. Fang, H. Zeng, T. Zhai, Y. Bando, D. Goldberg, Science of Advanced Materials 2 (2010) 273–294.

[6]Y.S. Chaudharya, A. Agrawala, R. Shrivastava, V.R. Satsangib, S. Dassa, Inter-national Journal of Hydrogen Energy 29 (2004) 131–134.

[7]M. Abaker, A. Umar, S. Baskoutas, S.H. Kim, S.W. Hwang, Journal of Physics D: Applied Physics 44 (2011) 1–7.

[8]H. Wang, J.-Z. Xu, J.-J. Zhu, H.-Y. Chen, Journal of Crystal Growth 244 (2002) 88–94.

[9]P.S. Dinesh, A. Naushad, Science of Advanced Materials 2 (2010) 295–335.

[10]L.P. Zhou, B.X. Wang, X.F. Peng, X.Z. Du, Y.P. Yang, Advanced Mechanical Engineering (2010) 1–4.

[11]Kirk-Othmer, in: J.I. Kroschwitz (Ed.), Encyclopedia of Chemical Technology, Wiley-Interscience, New York, 1999, p. 454.

[12]P. Massa, F. Ivorra, P. Haure, R. Fenoglio, Catalysis Letters 101 (2005) 201–209.

[13]S. Wei, Y. Chen, Y. Ma, Z. Shao, Journal of Molecular Catalysis A: Chemical 331 (2010) 112–116.

[14]G.Q. Yuan, H.F. Jiang, C. Lin, S.J. Liao, Journal of Crystal Growth 303 (2007) 400–406.

[15]H.J. Kim, V.I. Babushok, T.A. Germer, G.W. Mulholland, S.H. Ehrman, Journal of Materials Research 18 (7) (2003) 1614–1622.

[16]A. Aslani, V. Oroojpour, Physica B 406 (2011) 144–149.

[17]F. Bayansal, S. Kahraman, G. -Cankaya, H.A. -Cetinkara, H.S. G ¨uder, H.M. -C akmak, Journal of Alloys and Compounds 509 (2011) 2094–2098.

[18]Y. Zhang, S. Wang, X. Li, L. Chen, Y. Qian, Z. Zhang, Journal of Crystal Growth 291 (2006) 196–201.

[19]A. Manivel, S. Naveenraj, P.S. Kumar, S. Anandan, Science of Advanced Materials 2 (2010) 51–57.

[20]C.S. Dandeneau, Y.-H. Jeon, C.T. Shelton, T.K. Plant, D.P. Cann, B.J. Gibbons, Thin Solid Films 517 (2009) 4448–4454.

[21]H.Y. Bae, G.M. Choi, Sensors and Actuators B: Chemical 55 (1999) 47–54.

[22]J.D. Choi, G.M. Choi, Sensors and Actuators B: Chemical 69 (2000) 120–126.

[23]J.X. Wang, X.W. Sun, Y. Yang, K.K. Kyaw, X.Y. Huang, J.Z. Yin, J. Wei,

H.V. Demir, Nanotechnology 22 (2011) 1–7.

[24]F. Pola-Albores, F. Paraguay-Delgado, P. Ame´ zaga-Madrid, E. Ríos-Valdovinos, W.Antuúnez-Flores, M. Miki-Yoshida, Journal of Nanomaterials (2011). Article ID 643126.

[25]J. Rodríguez-Carvajal, Journal of Physics B: Atomic, Molecular and Optical Physics 192 (1993) 55–69.

[26]R.D. Bonetto, P.E. Zalba, M.S. Conconi, M. Manassero, Andean Geology 30 (2003) 103–115.

[27]W. Kraus, G. Nolze, Journal of Applied Crystallography 29 (1996) 301–303.

[28]P.D. Morgan, D.E. Partin, B.L. Chamberland, M. O'Keeffe, Journal of Solid State Chemistry 121 (1996) 33–37.

[29]J.R. Neumann, T. Zhong, Y.A. Chang, Bulletin of Alloy Phase Diagrams 5 (2)(1984) 136–140.

[30]A. Thobor, J.F. Pierson, Materials Letters 57 (2003) 3676–3680.

[31]J. Medina-Valtierra, C. Frausto-Reyes, G. Camarillo-Martı´nez, J. Ramı´rez-Ortiz, Applied Catalysis A: General 356 (2009) 36–42.

[32]D.R. Lide (Ed.), CRC Handbook of Chemistry and Physics, 77th ed., CRC Press, Boca Rato´ n, FL, 1996. p. 90 (Chapter 12).

[33]M.W. Chase, C.A. Davies, J.R. Downey, D.J. Frurip, R.A. McDonald, A.N. Syverud, NIST JANAF Thermochemical Tables, 1985 /http://kinetics.nist. gov/janaf/S (accessed September 2011).